Influence of Tip Clearance on Cavitation Characteristics of an Inducer of Turbopump: CFD Study

Authors:

Huan Han, Le Xiang, Kaifu Xu, Da Geng, Zibo Ren, Guohong Wu, Shuhong Liu, Zhigang Zuo

Date Submitted: 2023-02-17

Keywords: inducer, tip clearance, tip leakage, rotating cavitation, blade loading, radial force

Abstract:

> The tip clearance, a compact gap between the inducer blade tip and casing wall, is critical to both the liquid leakage and cavitation-induced forces of a turbopump. In this study, we numerically investigate the effect of tip clearance on the cavitation characteristics of an inducer. Six different tip clearances, 0.1, 0.3, 0.5, 1.0, 1.5, and 2 mm, namely Models A?F, were designed to evaluate the cavitation performance, cavity structure, blade loading, radial force, etc. Model D (1.0 mm) had the relatively highest head coefficient and smallest cavity area on each blade as compared to all other models. The pressure coefficient distribution and blade loading further confirmed that Model D can maintain a higher pressure head and better suppress the cavitation onset than the other models. The radial force signals in the time and frequency domains show that Model D has an intermediate force magnitude with slightly higher noises at the rotating frequency and its harmonic frequencies. Model D also has a relatively smaller vortex region and smaller vortex strength (?2 criterion). In short, all results show that Model D is the best alternative to balance the complex interactions of the bulk flow and tip leakage flow, compromising the hydraulic head and rotating cavitation.

Record Type: Published Article

Submitted To: LAPSE (Living Archive for Process Systems Engineering)

Citation (overall record, always the latest version):	LAPSE:2023.0088
Citation (this specific file, latest version):	LAPSE:2023.0088-1
Citation (this specific file, this version):	LAPSE:2023.0088-1v1

DOI of Published Version: https://doi.org/10.3390/pr11010055 processes

MDPI

Article

Influence of Tip Clearance on Cavitation Characteristics of an Inducer of Turbopump: CFD Study

Huan Han [1], Le Xiang [2], Kaifu Xu [2], Da Geng [1], Zibo Ren [1], Guohong Wu [1], Shuhong Liu [1,*] and Zhigang Zuo [1,*]

[1] State Key Laboratory of Hydroscience and Engineering, Department of Energy and Power Engineering, Tsinghua University, Beijing 100084, China
[2] Xi’an Aerospace Propulsion Institute, Xi’an 710100, China
* Correspondence: liushuhong@mail.tsinghua.edu.cn (S.L.); zhigang200@mail.tsinghua.edu.cn (Z.Z.); Tel.: +86-10-62773947 (Z.Z.)

Abstract: The tip clearance, a compact gap between the inducer blade tip and casing wall, is critical to both the liquid leakage and cavitation-induced forces of a turbopump. In this study, we numerically investigate the effect of tip clearance on the cavitation characteristics of an inducer. Six different tip clearances, 0.1, 0.3, 0.5, 1.0, 1.5, and 2 mm, namely Models A–F, were designed to evaluate the cavitation performance, cavity structure, blade loading, radial force, etc. Model D (1.0 mm) had the relatively highest head coefficient and smallest cavity area on each blade as compared to all other models. The pressure coefficient distribution and blade loading further confirmed that Model D can maintain a higher pressure head and better suppress the cavitation onset than the other models. The radial force signals in the time and frequency domains show that Model D has an intermediate force magnitude with slightly higher noises at the rotating frequency and its harmonic frequencies. Model D also has a relatively smaller vortex region and smaller vortex strength (λ_2 criterion). In short, all results show that Model D is the best alternative to balance the complex interactions of the bulk flow and tip leakage flow, compromising the hydraulic head and rotating cavitation.

Keywords: inducer; tip clearance; tip leakage, rotating cavitation; blade loading; radial force

check for updates

Citation: Han, H.; Xiang, L.; Xu, K.; Geng, D.; Ren, Z.; Wu, G.; Liu, S.; Zuo, Z. Influence of Tip Clearance on Cavitation Characteristics of an Inducer of Turbopump: CFD Study. *Processes* **2023**, *11*, 55. https://doi.org/10.3390/pr11010055

Academic Editor: Ambra Giovannelli

Received: 26 November 2022
Revised: 17 December 2022
Accepted: 21 December 2022
Published: 26 December 2022

1. Introduction

An inducer is a type of helico-axial pump installed upstream of the main pump (turbopump) to maintain the propulsion performance and suppress the cavitation damage in a liquid rocket engine. Due to the unstable force impulse and strong thermal effect during the cavitation bubble growth and collapse, the cavitation damage may eventually lead to a performance drop and severe vibrations and noises of the turbopump [1–7]. A number of studies have focused on the effects of the geometric parameters of case-based inducer configurations on the hydraulic performance and cavitation characteristics [8–12]. More typically, a multi-objective optimization method can be adopted to generate an optimal combination of the input parameters [13,14]. As the results emphasize, the tip clearance, a compact gap between the inducer blade tip and casing wall, is critical to both the liquid leakage and cavitation-induced forces [15–18].

On the other hand, the effects of the tip clearance change have been widely tested, since it is much easier to realize in practice, compared with other geometric modifications of the inducer. Casing walls with different grooves (e.g., J-shaped groove, circumferential groove, helical groove) have been proposed to effectively suppress the cavitation formation and growth [19–21]. Step casings have also been designed to evaluate their effects on the hydraulic performance and cavitation instabilities [11,22–24]. It is found that both the cavitation onset and the pumping head are sensitive to the starting location and the enlargement size of the steps. However, the underlying flow mechanisms remain unclear. The aforementioned studies of non-straight casing walls, e.g., groove casing and step casing, have further revealed that the local tip clearance might be one important factor for further development of a case-based inducer.

Since the non-straight casing wall can be viewed as a combination of several straight casing sections, a study of the tip clearances of straight casing walls may give a more fundamental understanding of their effects. A relatively large number of studies have been conducted to estimate the effect of the tip clearance of straight casing walls on the cavitation suppression of an inducer with or without the main pump [15–18,25–29]. However, due to the limited range of the tip clearances involved, some conclusions still need further validation. In particular, how the tip leakage interacts with the bulk flow in the inter-blade flow passages and how it influences the cavitation characteristics and the force distributions on the inducer and casing wall are still in need of further discussions. To this aim, a wide range of six different tip clearances were designed for the evaluation of a model inducer in this paper. The effects of the tip clearance on the hydraulic performance and cavitation cavities were analyzed via the discussion of the pressure distribution, the blade loading, and the radial force on the model inducer in detail.

The main structure of this paper is arranged as follows. The methodologies including the numerical schemes and experimental system are described in detail in Section 2. The numerical validation, the illustrated results of flow fields, and the mechanism analyses are conducted in Section 3. The discussions and conclusions are presented in the last section.

2. Materials and Methods

We describe the numerical schemes, geometrical characteristics, mesh topology, and experimental system involved in the current study in this section. Additionally, the design of six tip clearances, the mesh independence, and the difference of the experimental elbow tube and numerical straight tube downstream the inducer are described in detail.

2.1. Experimental Apparatus

To validate the numerical methodologies and results, our experiments were conducted in a recirculating water tunnel system established at Xi'an Aerospace Propulsion Institute. This typical closed-loop system consists of a drive motor, a booster pump, a water tank with the gas bladder inside, a honeycomb, a test section, pipelines, a degassing unit, the specific measurement instruments (flow meters, pressure sensors, water level indicator, etc.), and the valves. The motor is used to drive the inducer rotating at varying speeds in the operation conditions. The pump and tank control the flow rate and the pressure level. Additionally, the LED lighting system and high-speed cameras are arranged properly to visualize the spatio-temporal evolution of the flow behaviors of interest with a high resolution. More detailed information about the operation range and precision of test rig and the measuring technologies can be found in [18,25].

2.2. Inducer Geometry and Tip Clearance

The three-bladed model inducer involved in this study is shown in Figure 1. This model inducer has an equal pitch of the helical axial-flow blades. The geometric information and design operating conditions of this model inducer are listed in Table 1.

Table 1. Geometric characteristics of the tested three-bladed inducer.

Parameter	Value
Blade tip diameter, D_0 (mm)	100
Hub outlet diameter, D_1 (mm)	35.5
Hub inlet diameter, D_2 (mm)	15.5
Sweepback angle, α (°)	120
Number of blades, N	3

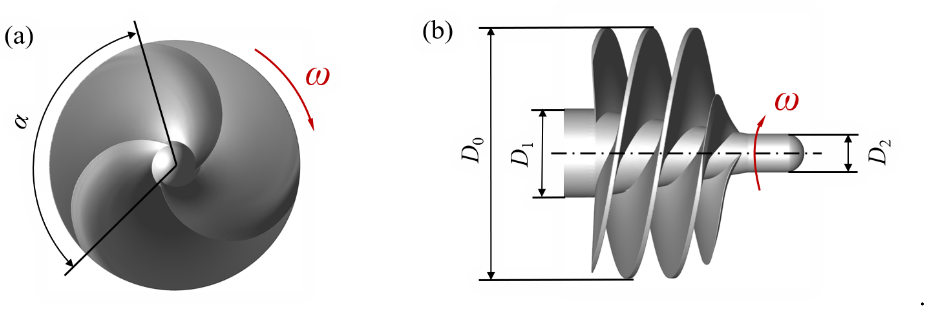

Figure 1. Schematic of the three-bladed model inducer in (**a**) front view and (**b**) side view.

A wide range of six different tip clearances, 0.1, 0.3, 0.5, 1, 1.5, and 2 mm, namely Models A–F, were designed to evaluate the geometric sensitivity of the tip clearance for our model inducer. The adoption of these clearances is based on, a tiny clearance, e.g., $\tau \leq 0.1$ mm, which challenges the manufacture and configuration in practice, and a large gap, which results in leaking the flow strongly, leading to significant hydraulic losses. In one previous study [30], the authors emphasized that the scale ratio (tip clearance-to-inducer blade tip diameter, τ/D_0) larger than 2% degrades the pumping head dramatically. The maximum tip clearance involved in our design is 2 mm, since the blade tip diameter D_0 of the model inducer is 100 mm in our study.

As shown in Figure 2, the schematic configuration of the inducer and casing wall with the tip clearance τ is illustrated. The casing model numbers and corresponding clearance are listed in Table 2. It is noted that the experimental validation of the numerical result was conducted for the case of τ = 0.5 mm (Model C), which is the original design of the tip clearance in practice for our test model inducer.

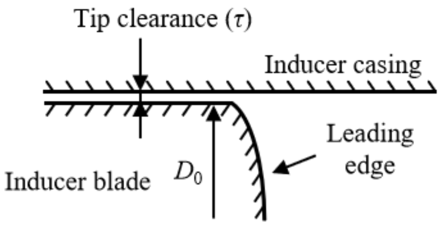

Figure 2. Schematic of tip clearance τ between blade tip and casing wall.

Table 2. Six tip clearances.

Model	Model A	Model B	Model C	Model D	Model E	Model F
τ (mm)	0.1	0.3	0.5	1.0	1.5	2.0

2.3. Mesh Topology and Numerical Scheme

The computational meshes and numerical simulations were conducted by the commercial software packages Pointwise and ANSYS CFX, respectively. The details about the computational domain frame and division, mesh generation logic and distribution, fluid physical properties, boundary conditions, turbulence model, cavitation model, and solving schemes are described meticulously as follows.

The entire computational domain of the model inducer in a straight casing wall is schematically shown in Figure 3. Although the pipeline downstream the inducer has an elbow structure in the experiment, an economic simplification of a straight pipe has been widely adopted to reduce the unnecessary mesh concentrations of geometrical complexity. To prove the rationality of this simplification, the same elbow tube downstream the inducer in the experiment is duplicated in Section 2.4. The specific values of each parameter in Figure 3 are listed accordingly.

To accurately represent the flow field and relevant characteristics of both non-cavitation and cavitation conditions, the total length of the entire computation domain was assigned as about 21.7-times the inducer blade tip diameter D_0. The inlet and outlet were set far away (>8 D_0) from the rotating blades, respectively, to prevent boundary effects on the computational accuracy. The casing wall diameter D depends on the tip clearance τ involved in our estimation, while the inducer blade tip diameter D_0 was fixed as 100 mm in this study.

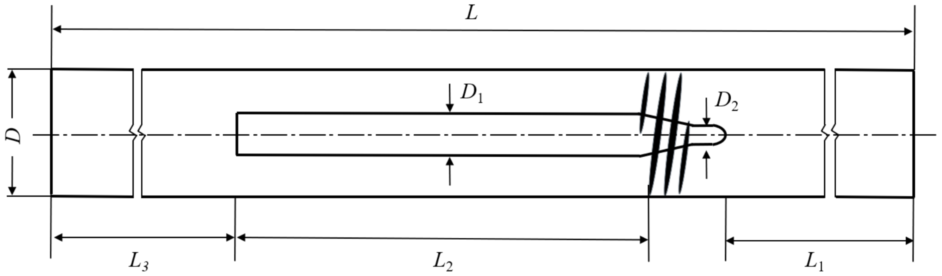

Figure 3. Entire computational domain. L = 2170 mm, L_1 = 800 mm, L_2 = 300 mm, L_3 = 1000 mm, $D = D_0 + 2\tau$, D_1 = 35.5 mm, D_2 = 15.5 mm.

Based on the typical mesh construction and division to simulate the fluid characteristics of a rotating fluid machine, the subdomains named rotational subdomains and stationary subdomains need to be properly arranged with the reasonable mesh resolution. A strategy of local refinement and smoothing was adopted on all wall surfaces (blades, shaft, casing, etc.). Based on the geometric complexity, hybrid unstructured meshes were generated. As shown in Figure 4, the detailed mesh distributions on the blade surfaces are demonstrated in two different views.

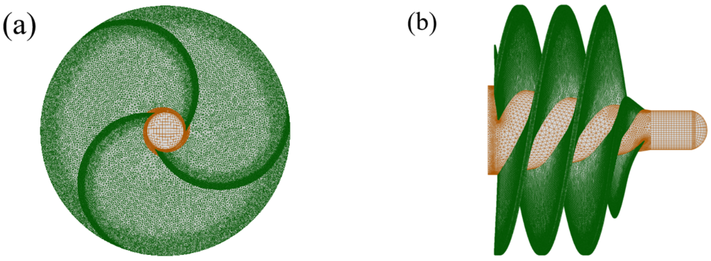

Figure 4. Detailed mesh distributions on the blade surfaces in (**a**) front view and (**b**) side view.

Finally, around 20 layers of prism meshes were generated, where the height of the first layer and the growing rate were set as 0.001 mm and 1.15, respectively. The above-mentioned mesh resolution ensures the accurate representation of the cavitation characteristics and instabilities on the inducer blades, tip clearance, and other solid surfaces. As the $k-\omega$ SST turbulence model typically requires, the $y+$ value was critically maintained at less than 10 for all computational cases throughout our study. Additionally, the grid independence test was conducted with six different mesh levels, and a moderate mesh resolution of 6.5 million grids was compromised by considering both the computational burden and accuracy. More details about the grid independence test can be found in our previous studies [11,24].

The Reynolds-averaged Navier–Stokes equations (RANS) were solved based on the concerned engineering interests. The turbulence model and cavitation model used in this study were the $k-\omega$ SST turbulence model and the Zwart–Gerber–Belamri (Z-G-B) cavitation model, respectively. The evaporation and condensation coefficients are user-defined values defined properly by the semi-empirical relationship validated by our previous studies. The volume of fluid (VOF) method was utilized for the mixture model of water and vapor through our cavitation simulations. The inlet and outlet boundaries of the computational domain are defined as the typical flow rate and static pressure types boundary conditions. A rigid and non-slip type wall was assumed on all the solid wall surfaces in this study.

The designed operation condition for the model inducer in this study was a rotating speed of 5000 r/min and a mass flow rate of 17.3 kg/s. The working medium was water as in the experiment, and the density and dynamic viscosity were then set as 1000 $\mathrm{kg/m^3}$ and 0.89 mPa·s, respectively. To promote the numerical convergence, a steady computation with 5000 iterations maximally was conducted first as the initialization condition of the following unsteady computation. According to the designed rotating speed of the model inducer, we performed 180 steps and 360 steps in one revolution for unsteady simulations separately. By compromising the efficiency and accuracy, the unsteady simulation for each case was conducted with 180 steps in one rotation period and, then, 20 iterations in each step.

2.4. Elbow Outlet

As mentioned in the previous subsection, an economic simplification of straight casing walls has been widely adopted instead of an elbow configuration downstream the inducer in experiments. We additionally estimated the difference between the ideal straight pipe and the elbow outlet. As shown in Figure 5, we exactly duplicated the same experimental configuration of an elbow tube downstream the inducer in our computational domain.

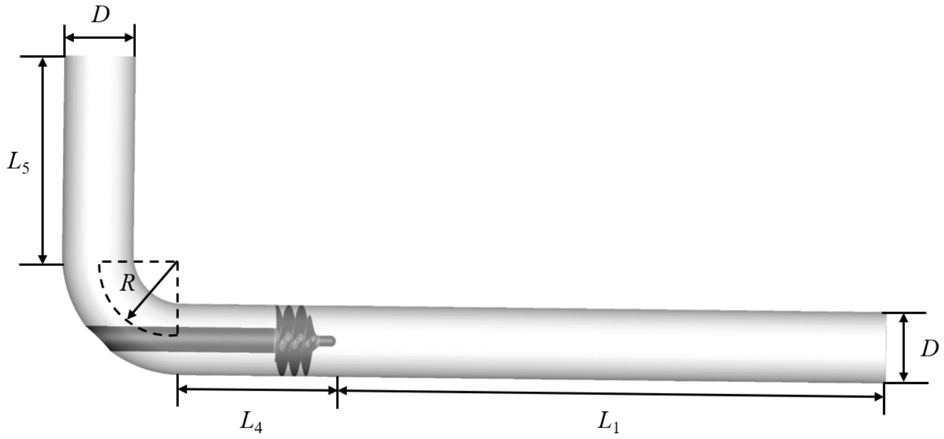

Figure 5. Computational domain of elbow configuration duplicated from the experiment system with the tip clearance of $\tau = 0.5$ mm. L_1 = 800 mm, L_4 = 220 mm, L_5 = 280 mm, D = 101 mm, R = 150 mm.

3. Results

3.1. Numerical Validation

In this subsection, two-fold numerical validations were performed. The first one aimed to confirm that the simplification of the straight pipe in the numerical simulation was rational to replace the complex elbow tube downstream the inducer in the experiment. The other one aimed to ensure that our adopted numerical methodologies and relevant schemes were well solved, representing the cavitation evaluations against the experimental measurements and observations.

As shown in Figure 6, the flow patterns (streamlines with the velocity magnitude), the pressure distribution on the axial section plane, as well as the cavity structure on the blade surfaces by steady computations were compared between the original elbow tube and the simplified straight tube. The cavity structure is visualized by the volumetric isosurfaces of vapor volume fraction α_v at 0.3. It is noted that the tip clearance was 0.5 mm for both configurations based on the experimental condition. In short, the comparisons proved that the result of the simplified straight tube had an acceptable agreement with the elbow configuration in the experiment.

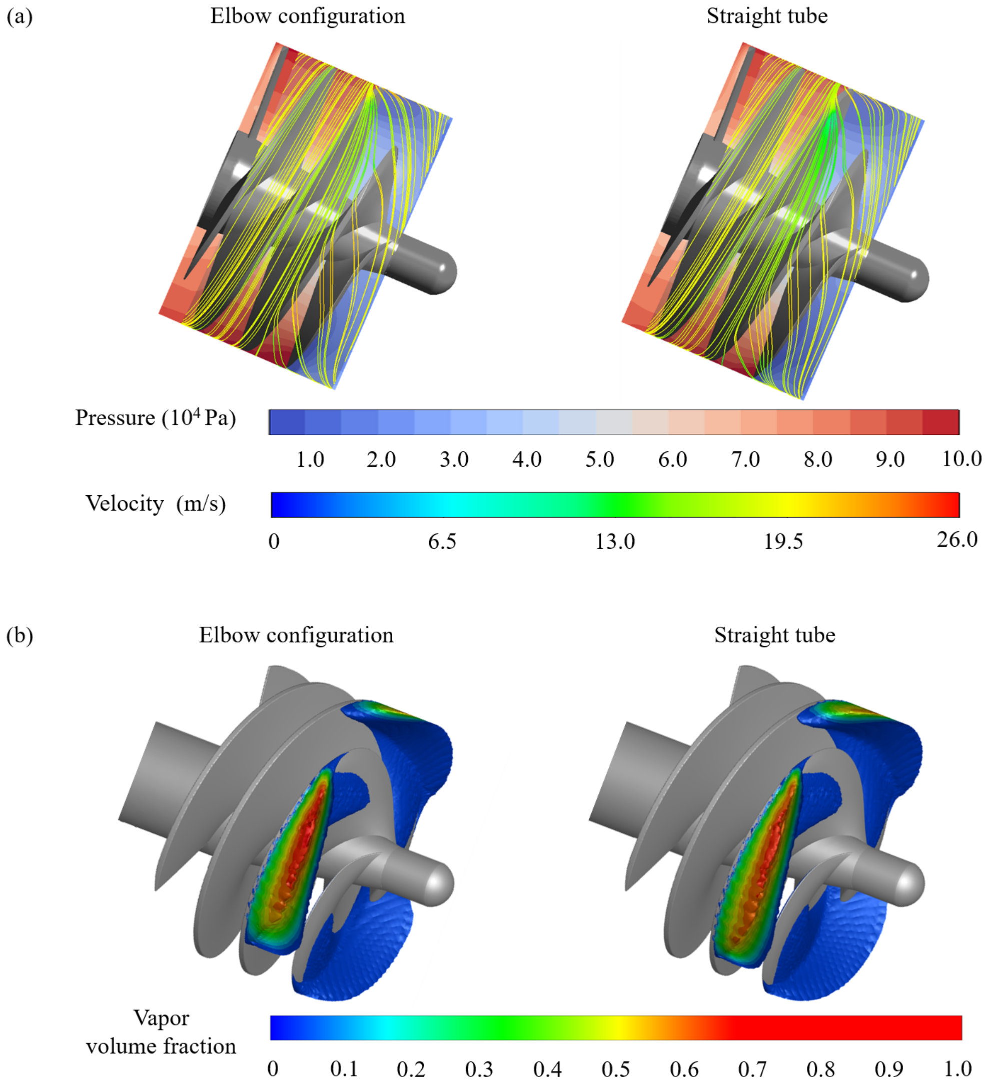

Figure 6. Steady numerical results between the elbow configuration and the simplified straight tube with the same tip clearance of 0.5 mm: (**a**) flow field (pressure distribution on the axial section plane, streamlines with the velocity magnitude) and (**b**) cavity structure with a vapor volume fraction of 0.3 on the blade surface.

Furthermore, we compared the experimental visualization and measurement with the unsteady simulation result of Model C. Both non-cavitation and cavitation performance tests were examined in the experiment and simulation. The non-cavitation test was conducted by tuning the inlet flow rate with a constant outlet pressure, while the cavitation test was conducted by tuning the outlet pressure with a constant inlet flow rate. Typically, the performance curves of hydraulic machinery are drawn in terms of three nondimensionalnumbers, flow coefficient Φ, head coefficient Ψ and cavitation number σ, as follows:

$$\Phi = \frac{Q}{\pi r_{tip}^2 V_{tip}}, \Psi = \frac{p_{out} - p_{in}}{0.5\rho V_{tip}^2}, \sigma = \frac{p_{in} - p_v}{0.5\rho V_{tip}^2}. \tag{1}$$

where Q, r_{tip}, V_{tip}, p_{in}, p_{out}, p_v, and ρ denote the flow rate, inducer blade radius, rotational velocity of the inducer blade tip, inlet static pressure, outlet static pressure, saturation vapor pressure, and water density at room temperature, respectively.

As shown in Figure 7, the non-cavitation and cavitation performance curves are plotted for Model C ($\tau = 0.5$ mm) in the experiment and simulation. The reference head coefficient Φ_{ref} is defined under the designed operation condition. By a direct comparison, the simulation results in both non-cavitation and cavitation tests showed good agreements with the experiment. The head coefficient in the non-cavitation test was slightly overestimated at the lower flow rate in the numerical prediction against the experiment. The simulated head in the cavitation test was slightly underestimated at only a few cavitation numbers compared to the experiment measurement. Our numerical simulations can well represent both the total performance trend and the cavitation breakdown points.

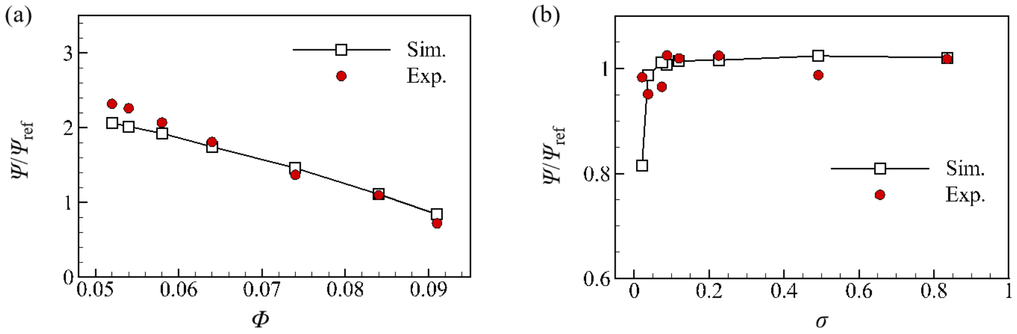

Figure 7. Performance comparison between experiment and simulation for Model C ($\tau = 0.5$ mm) in terms of: (**a**) non-cavitation performance and (**b**) cavitation performance.

To further validate that our numerical simulation can well predict not only the total performance, but also the flow field details in spatio-temporal evolution, the instantaneous cavity structures on the inducer blade surface were compared for experimental snapshots and simulation visualizations.

In Figure 8, we extract the experiment snapshots and corresponded numerical captures for Model C from eight even time intervals in one rotational period. The cavity structure in the simulation is represented by the volumetric isosurfaces of the vapor volume fraction up to 0.7. The numerical visualizations highly duplicate the cavity structure with respect to the videos taken by the high-speed camera in the experiment at the same instants. It is noted that the cavity structure and total volume size on each blade were observed as a fixed attachment synchronously as the blade rotates in both the experiment and simulation. In general, the above validations show that our simplified straight casing wall and adopted numerical processing are reliable to investigate the inducer performance and cavitation characteristics.

3.2. Effects of Tip Clearances

Since the numerical methodologies involved in our study were well validated, we now investigated the effects of tip clearance on the total hydraulic performance, the cavity structures, the blade loading, the radial force, the tip leakage flow, etc.

3.2.1. Cavitation Performance

As demonstrated in Figure 2 and Table 2, six different tip clearances (0.1–2 mm), Models A-F, were designed by expanding the casing wall diameter accordingly for our model inducer. The selection of these six gaps was based on the considerations of the challenges of manufacturing and configuration (small clearance), as well as the adverse impact of flow leakage (large clearance).

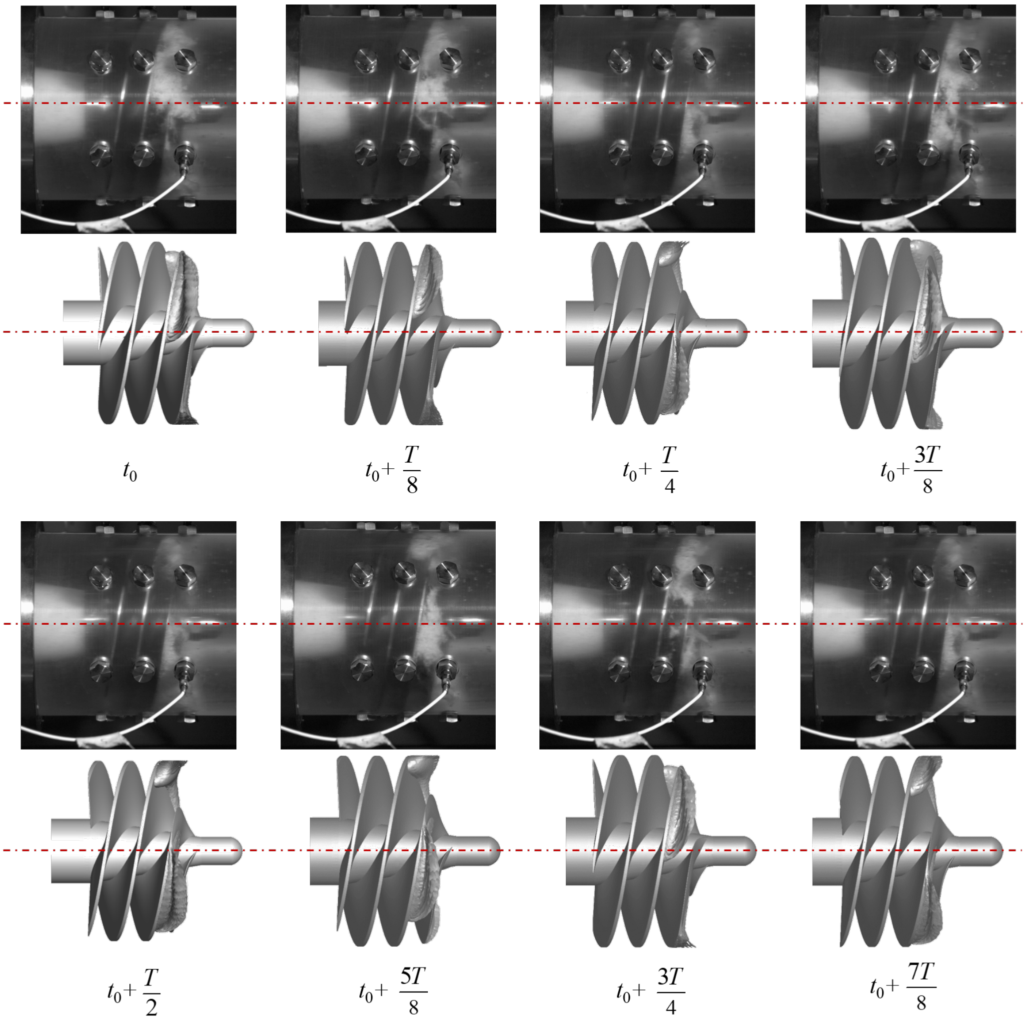

t_0 $t_0 + \frac{T}{8}$ $t_0 + \frac{T}{4}$ $t_0 + \frac{3T}{8}$

$t_0 + \frac{T}{2}$ $t_0 + \frac{5T}{8}$ $t_0 + \frac{3T}{4}$ $t_0 + \frac{7T}{8}$

Figure 8. Eight instantaneous captures of the cavity structure in one rotational period (T) between experiment (**top**) and simulation (**bottom**) for Model C ($\tau = 0.5$ mm).

We plot the cavitation performance curve at the designed operation condition for all six models in Figure 9. The designed operation condition for the model inducer in this study was at a rotating speed of 5000 r/min and a mass flow rate of 17.3 kg/s, while the inlet pressure and cavitation number were 27,000 Pa and 0.12, respectively. Since the head drops dramatically from $\tau = 0.5$ mm to $\tau = 0.3$ mm, we additionally computed another case of $\tau = 0.4$ mm for this performance curve. This case of $\tau = 0.4$ mm is only included in this figure, but not discussed further. The curve shows that the hydraulic head approaches the maximum when the tip clearance is 1 mm (Model D). Some remarks can be made as follows: (1) in the range of 0.1 mm $\leq \tau \leq$ 0.5 mm (Models A–C), the performance increases quasi-linearly as the tip clearance is enlarged; (2) the peak head is reached when the $\tau = 1$ mm (Model D); (3) the pumping head gradually drops as the tip clearance is enlarged from $\tau = 1$ mm to $\tau = 2$ mm (Models E–F).

From the above observations, it is revealed that a certain tip clearance, with the maximum hydraulic head, needs to be carefully estimated for our model inducer. The smaller tip clearances are more sensitive to the performance than the larger ones. The adverse effects of the tip clearances remain for the further interpolations by our following analyses.

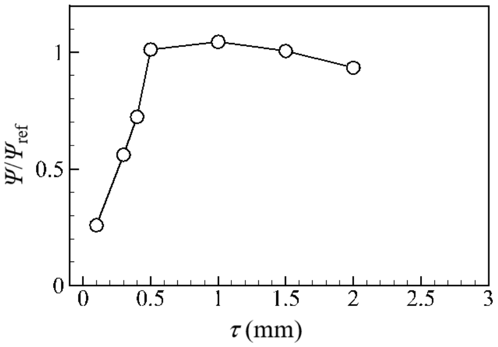

Figure 9. Cavitation performance for different clearances at the designed operation condition. The designed operation condition is at a rotating speed of 5000 r/min and a mass flow rate of 17.3 kg/s, while the inlet pressure and cavitation number are 27,000 Pa and 0.12, respectively.

3.2.2. Cavity Structures

As stated in Section 3.1, the cavity structures on three blades of Model C ($\tau = 0.5$ mm) were observed as the fixed attachments rotating synchronously as the blades rotated in both the experiment and simulation. First, we statistically extracted the monitoring data of the cavity area ($\alpha_v = 0.3$) on each blade of all models for several revolutions by post-processing analysis. The signals showed the same trends for all models: (1) the time-averaged magnitude of the cavity area on each blade was very similar for the three blades. (2) the temporary oscillation of the cavity area on each blade was relatively small compared to the time-averaged magnitude. (3) the phase difference of the temporary signal of the cavity area on each blade was almost fixed. The same observation can be seen in Figure 10 of [17]. Again, the above phenomena togethermay lead to a small resultant radial force on the model inducer, since the force component on each blade is almost counteracted in each direction.

One typical instant of the cavity structure is then extracted for all six models in Figure 10. The cavity is presented as the volumetric isosurface of $\alpha_v = 0.3$. For the two smallest tip clearance Models A ($\tau = 0.1$ mm) and B ($\tau = 0.3$ mm), the cavity size is much larger than the other four models, implying a larger area of the low pressure ($\leq p_v$) region on the blade suction side (SS). The cavity obviously extends from the blade tip to the mid-span, obstructing the inter-blade bulk flow and tip leakage flow for Models A–B. Models C–E have a similar pattern of cavity structures, while Model C has a slightly smaller area among the three models. Model F shows the different behaviors of all the models. Even the cavity area is small at the blade tip, and there is a certain portion of tailed cavity expanded in the spanwise direction.

The observations can be described by the coupling interaction of the bulk flow in the inter-blade passages and tip leaked flow. A proper tip clearance compromises the cavitation damage and hydraulic head with a certain tip leakage, and our case study suggests that the tip clearance of $\tau = 1.0$ mm (Model D) is the preferential design based on the model inducer involved in this paper.

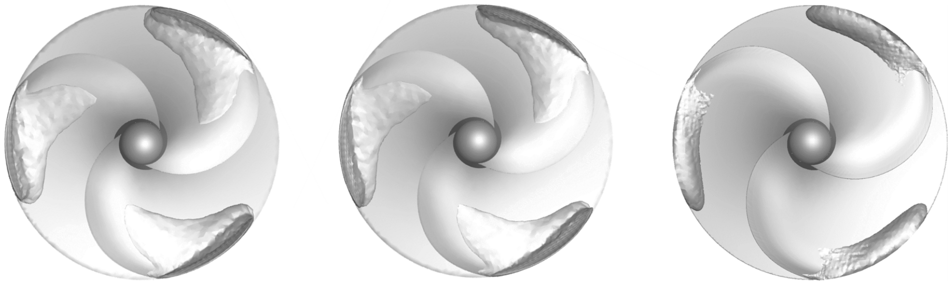

Model A (0.1 mm) Model B (0.3 mm) Model C (0.5 mm)

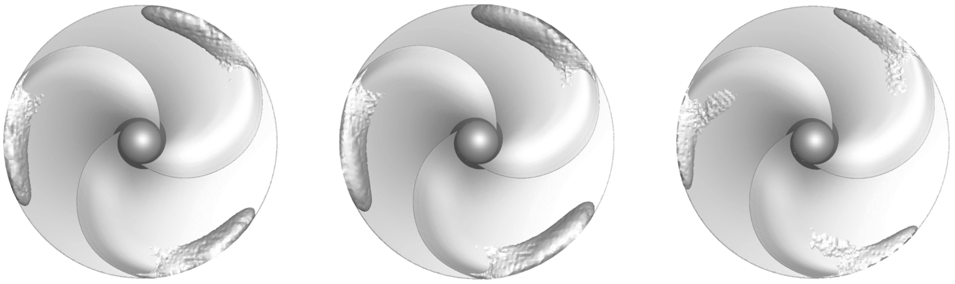

Model D (1.0 mm) Model E (1.5 mm) Model F (2.0 mm)

Figure 10. A typical instant of cavity structures at a vapor volume fraction of 0.3 for all six models.

3.2.3. Blade Loading and Force Distribution

After the inspection of the cavity structures on the blade surface, the forces exerted on the model inducer with six tip clearances were analyzed in detail. As described above, by the coupling interaction of the rotating blades and the fixed casing wall, the working medium is naturally pressurized, flowing through the inter-blade passages (bulk flow) and the compact space of the tip clearance (leakage flow). The working flow, especially the cavitation flow, then interacts with the inducer and casing wall with a certain pressure force, resulting in mechanical instabilities and noises.

The blade loading on both the pressure side (PS) and suction side (SS) of one certain blade for all six tip clearances is displayed in terms of the pressure coefficient $C_p = \frac{p - p_{inlet}}{0.5\rho V^2}$ in Figure 11, where p and V are locally the pressure and velocity at each location. In general, the net difference of the pressure coefficient from SS to PS determines the pumping capacity (hydraulic head), while the low-pressure regions at the SS, especially in the vicinity of the leading edge (LE), are highly related to the cavitation onset and evolution. In the C_p contour plot, Model C ($\tau = 0.5$ mm) shows the highest pressure difference from the LE to the 12 o'clock position clockwise, and Model D ($\tau = 1.0$ mm) shows the highest pressure difference from 12 o'clock to the trailing edge (TE). The above observations can be supported by the performance curve of Figure 9. Furthermore, Model D has a higher pressure distribution on the SS, especially in the the vicinity of the LE and blade tip, implying the suspension of rotating cavitation compared to the other models. Again, Model D shows a higher hydraulic head and lower cavity size compared to the five other models, and the results are consistent with Figures 9 and 10 shown in the above subsections.

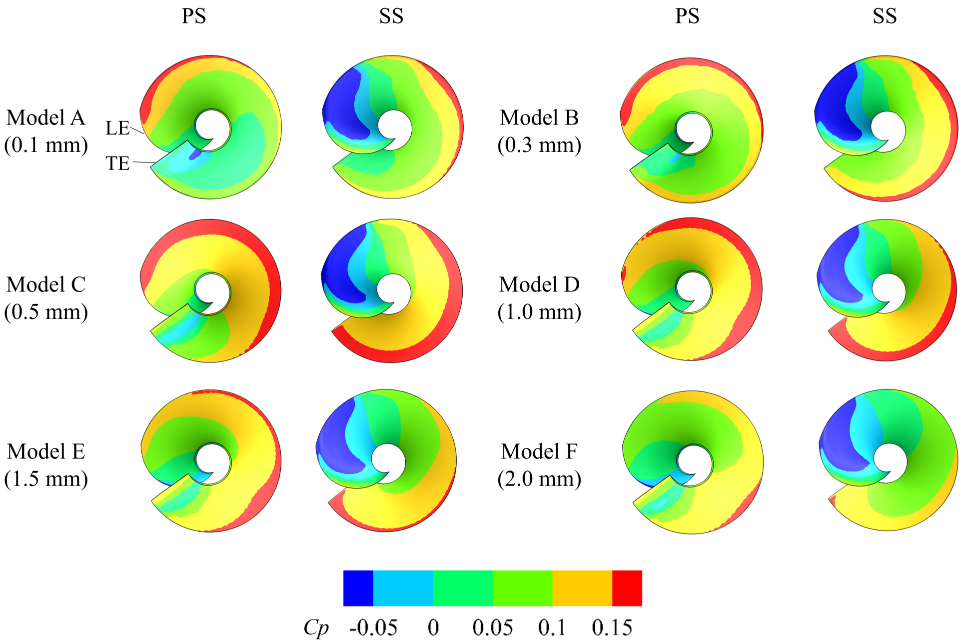

Figure 11. Loading at one certain blade for all models. LE: leading edge; TE: trailing edge; PS: pressure side; SS: suction side.

A cylindrical surface at 90% spanwise height was extracted with the contours of the C_p distribution and, then, flattened into a 2D surface in Figure 12 accordingly. Since this spanwise height is located around the blade tip of the cavitation onset zone, our selection aimed to closely track the blade loading characteristics impacted by the cavitation. From a total view, the pressure distribution is periodically pitched at the three blades for all Models A–F, reflecting the highly symmetric forces exerted on each blade. The pressure difference across the blade from the SS to the PS is the work on the flow performed by inducer pumping. The results again show that Models C and D have a higher head than the four other models. In detail, Model D has less pressure difference in the vicinity of the LE as compared to Model C, which may lead to a weak flow of tip leakage. Integrating Figures 9–11, the results further confirm that Model D of $\tau = 1.0$ mm has the best performance output relying on the complex interaction of inter-blade flow (bulk flow) and tip leakage flow induced by the rotating blades and fixed casing wall.

The integral of the C_p distribution on the blade surfaces implies the total force exerted on the inducer, and the radial component is the radial force leading to the rotating cavitation instability. We tracked the radial force on the three blades in 10 revolutions for all Models A–F to inspect the signal spectra in the time and frequency domains, respectively. The radial force of each model was first normalized by the time-averaged amplitude of Model C ($\tau = 0.5$ mm) and then presented as the orbital distribution, time series signals, and fast Fourier transform (FFT) frequency spectra accordingly.

As shown in Figure 13a, the normalized time-averaged radial force is plotted. It shows a similar trend to the performance curve, but the maximum is reached for Model C ($\tau = 0.5$ mm). The time-averaged radial force of Models A–B is about 20–30% of Model C, while it is about 60–70% for Models D–F. The orbit of the radial force, in Figure 13b, shows anonuniform distribution for all models. Model C has the highest radial force compared to all other cases, while Model A has the lowest radial force. Models D and E have similar magnitudes, but have relatively different orbital fluctuations. Model F shows an intermediate performance in terms of magnitude and orbital fluctuations.

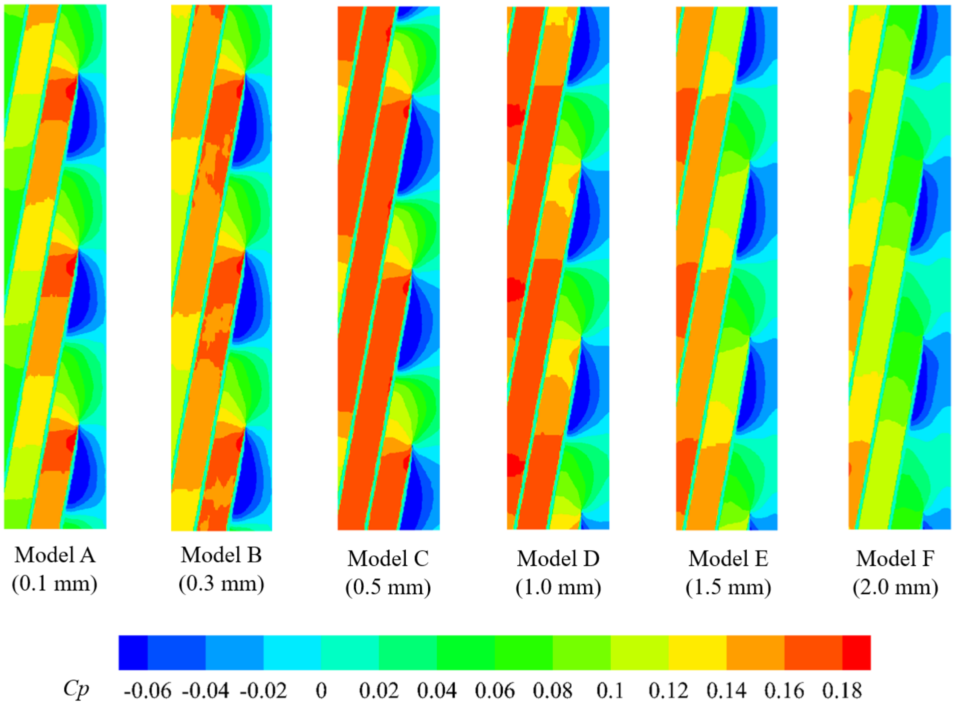

Figure 12. Loading on one blade for all six models.

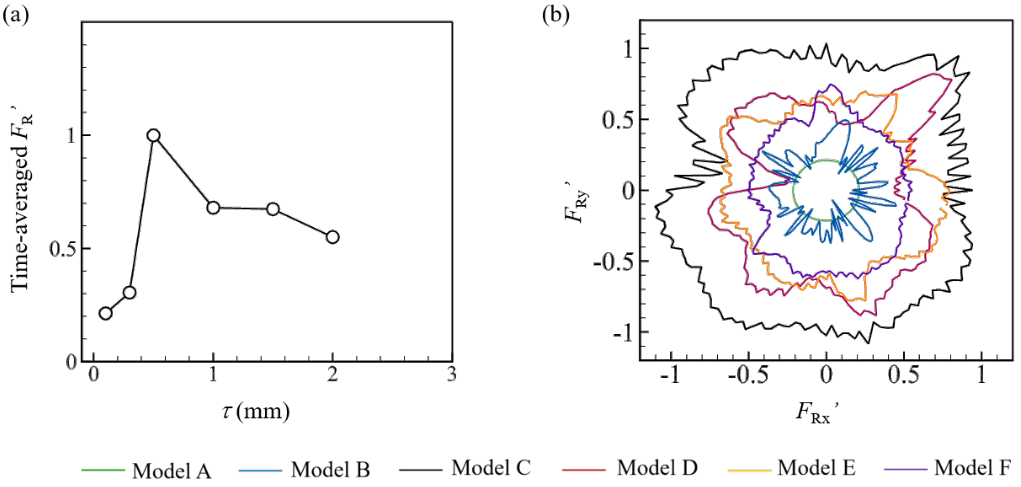

Figure 13. Normalized radial force for all six models as: (**a**) time-averaged magnitude; (**b**) orbital tracking.

In Figure 14a, the radial force signals of all six models show highly periodic characteristics in the time domain with the different time-averaged magnitudes. The peak radial force increases rapidly as the tip is enlarged when the tip clearance is in the range of 0.1–0.5 mm, while the peak radial force gradually drops when the tip clearance is within the range of 0.5–2 mm. The frequency spectra of the radial force is accordingly plotted by the FFT from the signals in the time domain, as shown in Figure 14b. Since the model inducer is a three-bladed helico-axial pump rotating at 5000 r/min in our study, the rotational frequency f_0 and blade passing frequency (BPF) ($3f_0$) are about 83.3 Hz and 250 Hz, respectively. In general, the peak amplitudes of the radial force for each model can be predicted at a frequency of f_0 and its harmonic frequencies (up to $3f_0$ involved in this study). Model A only has an obvious peak amplitude at f_0. Model B has three similar peak amplitudes at f_0, $2f_0$, and $3f_0$. Models C–F have a relatively similar trend to each other, with the amplitude at $2f_0$ higher than the others. For Model D, the amplitudes at f_0, $2f_0$, and $3f_0$ are higher than the others. In this sense, Model D may induce slightly sharp radial force noises at the rotational frequency and harmonic frequencies.

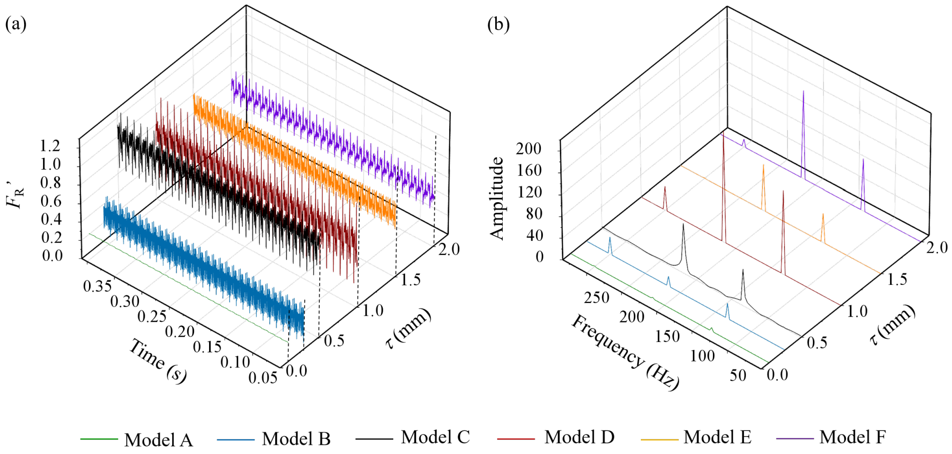

Figure 14. Normalized radial force for all six models in: (**a**) time domain; (**b**) frequency domain.

3.2.4. Flow Leakage

To better understand the overall interaction of bulk flow and tip leakage, the streamlines with the vortex strength (λ_2 criterion [31]) zoomed into the tip clearance region of the axial section are plotted in Figure 15. As described previously in this study, an optimized tip clearance for a certain inducer case could be compromised with the hydraulic head and the rotating cavitation instability. The proper leakage can effectively suppress the cavitation by resisting the lower pressure (magnitude level and occupied area) at the SS induced by the inducer rotating, while the high pressure in the PS can be properly maintained. The leakage flow is fully determined by the reverse pressure gradient across the SS to the PS, coupling with the tip clearance space when the flow rate and rotating speed are fixed.

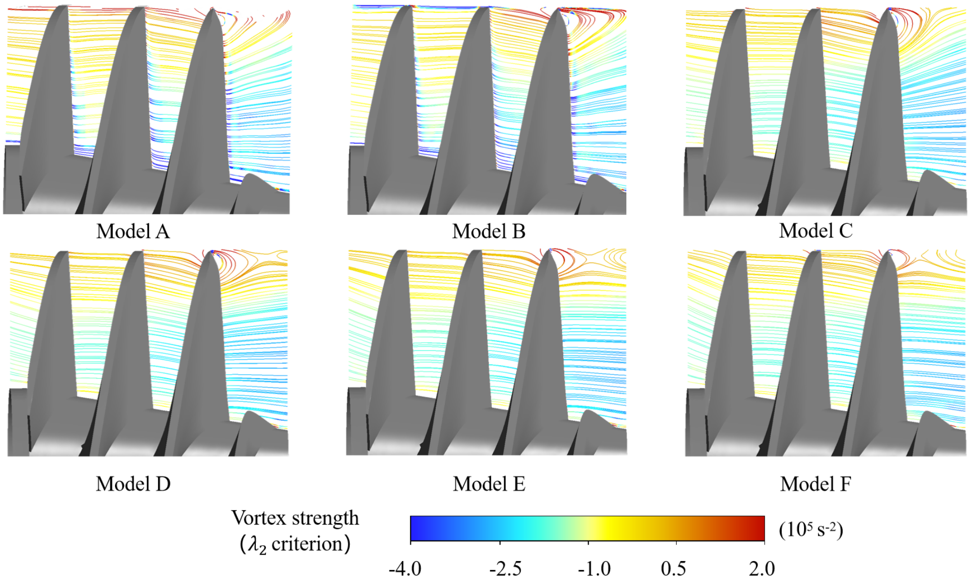

Figure 15. Streamlines with vortex strength (λ_2 criterion) for all models.

Tip leakage flow usually forms a certain pattern of vortex flow in terms of size and intensity. In Figure 15, Models A and B show the highest leakage flow vortex level and area, especially at the cavitation onset region, among all models, while the leakage vortex at the downstream is lower in Model B as compared with Model A. Model C shows slightly higher vortex intensity and area than Models D–F in the cavitation onset region. Model D is observed to have a relatively lager vortex size, but lower intensity compared to Models E and F. Overall, Model D with a tip clearance of 1.0 mm can be regarded as the relatively best alternative, balancing the tip leakage and bulk flow.

4. Conclusions

In this study, we numerically evaluated the effect of six different tip clearances, 0.1, 0.3, 0.5, 1, 1.5, and 2 mm, namely Models A–F, on the cavitation characteristics and hydraulic performance for a model inducer.

The numerical validation was first conducted for the casing as Model C ($\tau = 0.5$ mm) against the experimental result in terms of the instantaneous cavitation flow pattern, the non-cavitation and cavitation performance curves. We then investigated the cavitation performance under the designed operation condition for all six models. The performance curve shows that the hydraulic head approached the maximum when the tip clearance was 1 mm (Model D). Furthermore, the integration of the cavity structure and blade loading on the blade surfaces showed that Model D had the smallest cavity size among all six models. The above observations can be explained by the relatively higher pressure distributions on both the pressure side and the suction side, especially in the vicinity of the LE and the blade tip.

The radial force was referred to the rotating cavitation instability in this study. The radial force increased rapidly when the tip clearance was within the range of 0.1–0.5 mm, while the radial force then gradually dropped as the tip enlarged when the tip clearance was in the range of 0.5–2 mm. The frequency spectra of the radial force showed that the amplitudes at f_0, $2f_0$ and $3f_0$ for Model D were higher compared to the others, which may induce the slightly sharp radial force noises.

Finally, we zoomed into a specific view of the tip clearance region on the axial section plane. Model D was observed with an intermediate vortex size, but lower intensity among all models. Overall, Model D with a tip clearance of 1.0 mm can be regarded as the relatively best alternative, balancing the tip leakage and bulk flow, in our study. The workflow and analysis of this paper may provide a baseline reference to efficiently evaluate the effect of tip clearance on the cavitation characteristics of an inducer.

Author Contributions: Conceptualization, Z.Z., S.L., H.H., X.L. and K.X.; methodology, Z.Z., S.L. and H.H.; software, H.H., D.G. and G.W.; investigation, H.H.; data analysis, H.H. and D.G.; writing—original draft preparation, H.H., L.X., Z.R. and G.W.; writing—review and editing, L.X., K.X., S.L. and Z.Z.; visualization, H.H. and D.G.; supervision, S.L. and Z.Z.; project administration, Z.Z. All authors have read and agreed to the published version of the manuscript.

Funding: This research was funded by the National Natural Science Foundation of China (NSFC, No. 52079066 and No. 52076120), the State Key Laboratory of Hydroscience and Engineering (Nos. 2019-KY-04, sklhse-2020-E-05, and sklhse-2020-E-03), and the China Postdoctoral Science Foundation (2022M711766).

Data Availability Statement: Data not available to be shared due to the technical limitations.

Conflicts of Interest: The authors declare no conflict of interest.

References

1. Ge, M.; Ptekovsek, M.; Zhang, G.; Jacobs, D.; Coutier-Delgosha, O. Cavitation dynamics and thermodynamic effects at elevated temperatures in a small Venturi channel. *Int. J. Heat Mass Tran.* **2021**, *170*, 120970. [CrossRef]
2. Ge, M.; Manikkan, P.; Ghossein, J.; Subramanian, R.K.; Coutier-Delgosha, O.; Zhang, G. Dynamic mode decomposition to classify cavitating flow regimes induced by thermodynamic effects. *Energy* **2022**, *254*, 124426. [CrossRef]
3. Ge, M.; Zhang, G.; Ptekovsek, M.; Long, K.; Coutier-Delgosha, O. Intensity and regimes changing of hydrodynamic cavitation considering temperature effects. *J. Clean Prod.* **2022**, *338*, 130470. [CrossRef]
4. Ge, M.; Sun, C.; Zhang, G.; Coutier-Delgosha, O.; Fan, D. Combined suppression effects on hydrodynamic cavitation performance in Venturi-type reactor for process intensification. *Ultrason. Sonochem.* **2022**, *86*, 106035. [CrossRef]

5. Zuo, Z.; Zhang, H.; Ren, Z.; Chen, H.; Liu, S. Thermodynamic effects at Venturi cavitation in different liquids. *Phys. Fluids* **2022**, *34*, 083310. [CrossRef]
6. Zhang, H.; Chen, H.; Xiang, L.; Zuo, Z.; Liu, S. Instabilities of blow-down type Venturi cavitation considering thermodynamic effect. *Thermophys. Aeromech.* **2021**, *28*, 563–576. [CrossRef]
7. Zhang, H.; Zuo, Z.; Mørch, K.A.; Liu, S. Thermodynamic effects on Venturi cavitation characteristics. *Phys. Fluids* **2019**, *31*, 097107.
8. Horiguchi, H.; Semenov, Y.; Nakano, M.; Tsujimoto, Y. Linear stability analysis of the effects of camber and blade thickness on cavitation instabilities in inducers. *J. Fluids Eng.* **2006**, *128*, 430–438. [CrossRef]
9. Guo, X.; Zhu, Z.; Cui, B.; Shi, G. Effects of the number of inducer blades on the anti-cavitation characteristics and external performance of a centrifugal pump. *J. Mech. Sci. Technol.* **2016**, *30*, 3173–3181. [CrossRef]
10. Cheng, X.; Li, Y.; Zhang, S. Effect of inlet sweepback angle on the cavitation performance of an inducer. *Eng. Appl. Comp. Fluid Mech.* **2019**, *13*, 713–723. [CrossRef]
11. Yu, L.; Zhang, H.; Chen, H.; Zuo, Z.; Liu, S. Numerical study on the influence of step-casing on caviting flows and instabilities in inducers with equal and varying pitches. *Processes* **2020**, *8*, 1103. [CrossRef]
12. Bi, C.; Li, J. Effect of radial height of helical static blade on the cavitation performance of inducer. *Appl. Sci.* **2022**, *12*, 3987. [CrossRef]
13. Parikh, T.; Mansour, M.; Thevenin, D. Maximizing the performance of pump inducers using CFD-based multi-objective optimization. *Struct. Multidiscip.* **2022**, *23*, 65.9. [CrossRef]
14. Yu, L.; Zhang, H.; Chen, H.; Li, Y.; Zuo, Z.; Liu, S. Geometric optimization of an inducer with respect to rotating cavaitation generated radial forces by using an orthogonal experiment. *J. Appl. Fluid Mech.* **2016**, *11*, 1591–1598.
15. Okita, K.; Ugajin, H.; Masutmoto, Y. Numerical analysis of the influence of tip clearance of on the unsteady cavitating flows in a three-bladed inducer. *J. Hydrodyn.* **2009**, *21*, 34–40. [CrossRef]
16. Fu, Y.; Yuan, J.; Yuan, S. Pace, G.; d'Agostino, L. Effect of tip clearance on the internal flow and hydraulic performance of a three-bladed inducer. *Int. J. Rotating Mach.* **2017**, 2329591. [CrossRef]
17. Xu, Y.; Tan, L.; Liu, Y.; Cao, S. Pressure fluctuation and flow pattern of a mixed-flow pump with different blade tip clearances under cavitation condition. *Adv. Mech. Eng.* **2017**, *9*, 1687814017696227. [CrossRef]
18. Xiang, L.; Tan, Y.; Chen, H.; Xu, K. Experimental investigation of cavitation instabilities in inducer with different tip clearance. *Chin. J. Aeronaut.* **2021**, *34*, 168–177. [CrossRef]
19. Fujii, A.; Uchiumi, M.; Kurokawa, J.; Tsujimoto, Y. Suppression of Rotating Cavitation in an Inducer by J-groove. *Trans. Jpn. Soc. Mech. Eng. Ser. B.* **2006**, *72*, 2496–2504. [CrossRef]
20. Kang, D.; Arimoto, Y.; Yonezawa, K.; Hironori, H.; Kawata, Y.; Hah, C.I.; Tsujimo, Y. Suppression of cavitation instabilities in an inducer by circumferential groove and explanation of higher frequency components. *Int. J. Fluid Mach. Syst. 2.* **2010**, *3*, 137–149. [CrossRef]
21. Li, X.; Hu, S.C.; Zhou, Y.J.; Xiao, L.M.; Liu, C.; Wang, J. Study on cavitation performance of an inducer with helical grooves (In Chinese). *J. Propuls. Technol.* **2020**, *41*, 553–558.
22. Fujii, A.; Azuma, S.; Yoshida, Y.; Tsujimoto, Y.; Uchiumi, M.; Warashina, S. Effects of inlet casing geometries on unsteady cavitation in an inducer. *Trans. Jpn. Soc. Mech. Eng. B.* **2004**, *16*, 1450–1458. [CrossRef]
23. Shimagaki, M.; Haga, H.; Hashimoto, T.; Wanatabe, M. Effect of casings configurations of on the internal flow and unsteady pressure fluctuation in a rocket pump inducer (in Japanese). *J. Jpn. Soc. Aeronaut. Space Sci.* **2005**, *53*, 266–273.
24. Han, H.; Geng, D.; Xiang, L.; Xu, K.; Ren, Z.; Liu, S.; Zuo, Z. Influence of step casings on the cavitation characteristics of inducers. *Processes* **2022**, *10*, 1598. [CrossRef]
25. Campos-Amezcua, R.; Khelladi, S.; Mazur-Czerwiec, Z.; Bakir, F.; Campos-Amezcua, A.; Rey, R. Numerical and experimental study of cavitating flow through an axial inducer considering tip clearance. *Proc. Inst. Mech. Eng. Part A J. Power Energy.* **2013**, *227*, 858–868. [CrossRef]
26. Guo, M.; Yang, S.; Li, X.; Shi, L.; Hua, E.; Zhu, Z. The tip clearance cavitation mechanism of a high-speed centrifugal pump with a splitter-bladed inducer. *Processes* **2021**, *9*, 1576. [CrossRef]
27. Guo, M.; Jiang, C.; Qian, H.; Shi, L.; Zhu, Z.; Zhou, C. Effect of tip clearance cavitation flow of a shunt blade inducer. *Energies* **2022**, *15*, 6330. [CrossRef]
28. Shen, J.; Xu, F.; Cheng, L.; Pan, W.; Ge, Y.; Li, J.; Zhang, J. Simulation of internal flow characteristics of an axial flow pump with variable tip clearance. *Water* **2022**, *14*, 1652. [CrossRef]
29. Shen, X.; Zhang, D.; Xu, B.; Wu, H.; Wang, P.; Shi, W. Comparative study of tip leakage vortex trajectory and cavitation in an axial flow pump with various tip clearances. *J. Mech. Sci. Technol.* **2022**, *36*, 1289–1302. [CrossRef]
30. Brennen, C.E. *Hydrodynamic of Pump*; Concepts ETI, Inc.: White River Junction, VT, USA, 1994; p.136.
31. Jeong, J.; Hussain, F. On the identification of a vortex. *J. Fluid. Mech* **1995**, *285*, 69–94. [CrossRef]